Mining tailings as a raw material for glass-bonded thermally sprayed ceramic coatings: microstructure and properties

Marjaana Karhu [a*], Juha Lagerbom [a], Mari Honkanen [b], Elina Huttunen-Saarivirta [a], Jarkko Kiilakoski [c], Petri Vuoristo [c], Soili Solismaa [d] and Päivi Kivikytö-Reponen [a]

[a] VTT Technical Research Centre of Finland Ltd, Visiokatu 4, P.O. Box 1300, 33101 Tampere, Finland

[b] Tampere Microscopy Center, Tampere University, Korkeakoulunkatu 3, 33014 Tampere University, Finland

[c] Thermal Spray Center Finland (TSCF), Tampere University, Faculty of Engineering and Natural Sciences, P.O. Box 589, 33014 Tampere, Finland

[d] Geological Survey of Finland, P.O. Box 1237, 70211 Kuopio, Finland

* Corresponding author: marjaana.karhu@vtt.fi, +358405365926

ABSTRACT

Magnesium aluminate, $MgAl_2O_4$, spinel powders for thermal spraying, were synthesized from secondary raw materials by spray drying and subsequent reaction sintering. Talc ore mining tailings and aluminium hydroxide precipitate from aluminium anodizing process were studied. A stoichiometric $MgAl_2O_4$ spinel coating was prepared as a reference using pure raw materials. Atmospheric plasma spraying resulted in the formation of ceramic coatings. Microstructural investigations revealed that the reference coatings exhibited crystalline lamellar microstructure of $MgAl_2O_4$ but secondary coatings contained amorphous areas between the crystalline $MgAl_2O_4$ clusters. Abrasive wear test results revealed considerably lower wear rate for secondary coatings. It is suggested that the different structure of coatings, particularly the high degree of amorphous phase between the isolated crystalline $MgAl_2O_4$ clusters caused the higher abrasive wear resistance by changing the wear mechanism. The dielectric breakdown strength of the secondary coatings were at the same level, 24 V/µm, as compared to reference coating, 23 V/µm.

Key words: $MgAl_2O_4$ spinel, mining tailings, circular economy, thermal spray, ceramic coating

1. INTRODUCTION

Magnesium aluminate spinel, $MgAl_2O_4$, is the only intermediate compound in the MgO-Al_2O_3 system [1]. It is a refractory oxide having useful physical, chemical and thermal properties, such as a high melting point (2135°C), excellent resistance against chemical attack and very good thermal characteristics, both at ambient and elevated temperatures. Due to these desirable properties, sintered $MgAl_2O_4$ spinel has a wide range of applications in structural, chemical, optical, and electrical industries, for example as a high-performance refractory material [2]. Magnesium aluminate spinel is also used in thermally sprayed ceramic coatings for harsh high-temperature environments and in electrical insulating applications where normal insulating materials, such as polymers, cannot be used [3][4]. It has been shown that magnesium aluminate spinel is stable during the thermal spraying process [5] and the only phase determined in the resulting coatings, as cubic $MgAl_2O_4$ [6]. Additionally to the good electrical insulation properties of spinel coatings [7] [8] [9] [10], the coatings have been reported to exhibit good mechanical properties [11].

Calcination of magnesite, $MgCO_3$, is the principal route to produce magnesium oxide, MgO, for the use as a ceramic raw material [12]. China, North Korea, and Russia account for 65% of global magnesite reserves, with China being the largest magnesite producer. For these reasons, magnesite was included in the 2014 EU "Critical Raw Materials" list [13] [14]. Simultaneously, as the consequence of the growth of mining and mineral processing industry, large volumes of mining wastes are being produced. Mining waste typically refers to an unwanted mining by-product but may still contain valuable constituents [15]. Mining tailings consist of fine-grained (1-600µm) ground-up rock residue after minerals of value have been extracted from mined ore. The physical and chemical characteristics of mining tailings vary considerably with ore type [16]. Overall, mining tailings are seen as one potential resource to be utilized on the way towards circular economy and resource efficiency [17].

In this paper, the sample of talc ore mining tailings was studied. Talc ore mining tailings are rich in magnesite [18] and then can be seen as potential ceramic raw material source. This paper investigates the feasibility of talc ore mining tailings as raw material source for thermally sprayed ceramic coatings. Here, $MgAl_2O_4$ spinel composition was aimed for. Because the sample of mining tailings does not contain aluminium enough for spinel composition, another secondary raw material, precipitate of aluminium hydroxide, $Al(OH)_3$, a by-product generated by aluminium anodizing process was studied. As a research hypothesis, agglomerated $MgAl_2O_4$ spinel-based powders, ideal for thermal spraying, could be synthesized by spray drying and subsequent reaction sintering using these secondary Mg and Al sources as raw materials. In order to investigate and establish a direct comparison in powders and resulting coatings, a stoichiometric $MgAl_2O_4$ spinel coating was prepared using commercially available primary raw materials. The sample of talc ore mining tailings was rich in magnesite >80% but contained also other minerals, such as talc, chlorite, dolomite and iron sulphide [18].The effect of constituents other than Mg and Al in mining tailings mineralogy on the resulting coatings was investigated as the main research question in this study. Finally, the properties and wear performance of the secondary and primary coatings were examined and correlated to their microstructures.

2. EXPERIMENTAL PROCEDURE

2.1 RAW MATERIALS

The mining tailings sample (10l bucket) from talc ore mine was taken from one point of the temporary storage pile. However, it should be noted that there exist to some extend quality variation for the entire mining tailings area as the mineralogy, grain size and chemistry of the tailings may vary in different parts of deposit due to differences in the original ore composition and separation during storage. Table shows the mineralogical analysis of the used talc ore tailings sample presenting the main identified minerals. Mineralogical characterization included the identification and quantification of mineral phases with scanning electron microscopy (SEM) together with elemental analyses by energy-dispersive spectrometry (EDS). The more detailed explanation of mineralogical analysis, chemical composition analysis, geochemical analysis and sampling procedure are described elsewhere [19]. Ismailov et al. [20] have shown that magnesite in the talc ore tailings was not stoichiometric $MgCO_3$ but had a varying amount of iron substituting magnesium in the lattice. Indeed, there exists a series of solid solutions between $MgCO_3$ and siderite, $FeCO_3$ [21]. Iron carbonate content in magnesite could lie between 0 and 5%. If iron carbonate content increases to the level between 5% and 30%, mineral is then called breunnerite [21].

Table 1. The main identified minerals of the talc ore tailings sample (% total volume).

Mineral	Sample vol%
Magnesite, $MgCO_3$	80.0
Talc, $Mg_3Si_4O_{10}(OH)_2$	9.4
Chlorite, $(Mg,Fe)_3(Si, Al)_4O_{10}$	4.9
Dolomite, $CaMg(CO_3)_2$	1.8

Error! Reference source not found. Table 2 presents the total concentration of cations (calculated as oxides) in the tailings sample, measured with X-ray fluorescence spectrometry (XRF). Loss of ignition (LOI) value presents the loss in weight after being heated to 1000°C.

Table 2. Chemical composition of the talc ore tailings sample (wt.%).

	MgO	**SiO_2**	**Fe_2O_3**	**CaO**	**Al_2O_3**	**LOI**
Talc ore tailings sample	38.5	10.1	8.2	0.8	0.61	42.7

Because the sample of talc ore tailings does not contain enough aluminium for synthesizing magnesium aluminate, $MgAl_2O_4$, spinel, another secondary raw material, an aluminium hydroxide precipitate, a by-product from aluminium anodizing process, was studied as alumina source. The precipitate composed mainly of gibbsite, aluminium oxide trihydroxide $Al(OH)_3$ and the elemental composition is shown in Table 3.

Table 3. Elemental composition of aluminium hydroxide precipitate (wt.%).

	O	**Al**	**H**	**S**	**Na**
Aluminium oxide precipitate	62.2	27.8	3.9	3.8	0.8

As a reference, pure magnesium aluminate $MgAl_2O_4$ spinel powder was prepared using commercially available MgO (99.9% purity) and boehmite, aluminium oxide hydroxide, AlO(OH) (99.99% purity) powders as raw materials. MgO powder was provided by Inframat and AlO(OH) powder was provided by Sasol Germany GmbH.

2.2 POWDER PREPARATION

Four experimental powder mixtures were prepared aiming at the synthesis of magnesium aluminate, $MgAl_2O_4$, spinel. Mixtures shown in Table were formulated with 1:2 Mg to Al molar ratio. Reference powder represents the reference composition, $MgAl_2O_4$ spinel powder, prepared using commercially available pure MgO and AlO(OH), as raw materials. SC100 powder represents the secondary $MgAl_2O_4$ powder composition, prepared using 100% only secondary raw materials, talc ore tailings sample and anodizing by-product aluminium hydroxide, $Al(OH)_3$. SC30 powder and SC60 powder represent compositional points between the composition of Reference and Secondary100 powders, prepared using both commercial and secondary sources of raw materials, approximately 30% secondary raw materials in SC30 powder and approximately 60% in SC60 powder.

Table 4. Test matrix compositions for the spinel powder synthesis experiments (wt. %).

Recipe code	MgO (commercial)	AlO(OH) (commercial)	Talc ore tailings sample (secondary)	By-product $Al(OH)_3$ (secondary)
Reference	25.1	74.9	-	-
SC30	16.8	50.0	11.7	21.7
SC60	8.40	25.0	23.4	43.4
SC100	-	-	35.0	65.0

The talc ore mining tailings sample was received in powder form having 90% (D90) of particle size below 140 µm. For powder mixture compositions, it was first ground by jet milling into the particle size below 10 µm in order to increase the reactivity and ensure mixing of the ingredients. Secondary alumina source had the particle size of 6.70 µm (D90). The average grain size of commercial reference MgO was below 1 µm, while that of AlO(OH) powder was below 0.77 µm, thus there was notable difference in the particle sizes of the raw material powders. In order to prepare agglomerated powders suitable for atmospheric plasma spraying, water-based ceramic powder suspensions (2 % Dispex A) were prepared from raw material mixtures by bead milling for 15 minutes. Before spray drying, an organic binder polyethylene glycol, PEG, 2%, was added to suspensions. Suspensions were dried with an industrial- scale spray dryer Niro Atomizer to produce agglomerated powders. Spray-dried powders were reaction-sintered in an ENTECH air chamber furnace in ambient air atmosphere and pressure at the temperatures between 1075°C and 1150°C.

2.3 COATING DEPOSITION

Atmospheric plasma spraying (APS) technique was used for the deposition of coatings. In a plasma spray gun, a direct current (DC) power is used for the generation of plasma. Energy is transferred into plasma-forming gases until the energy level is sufficient to ionize the gas. When the ionized gas returns back to atoms/molecules by recombining, a high amount of energy is released. The gas expands in the atmosphere and forms an extremely hot and high-velocity gas jet. The powder is injected radially to the plasma jet where the particles of the powder melt and get accelerated. The coating is formed when the melted and accelerated powder particles impact onto the substrate surface. [22]

In this study, coatings were sprayed with an APS ProPlasma gun (Saint Gobain, 6.5HighPower- mm nozzle) using argon/ hydrogen (Ar/H_2) plasma gas mixture. Spray distance was constant at 110 mm. The main spray parameters are summarized in Table 5. Coatings with the thickness range of 225 - 300 µm were deposited on grain-blasted carbon steel substrates. The plasma gun was robot-manipulated with 51 m/min surface speed and 3 mm increments.

Table 5. Main spray parameters.

Parameter	Value
Plasma gas mixtures Ar/H_2 (l/min)	43/12
Arc current (A)	600
Voltage (V)	76
Plasma power (kW)	45.4

2.4 CHARACTERIZATION TECHNIQUES

Phase structure analyses were performed for both synthesized powders and deposited coatings using X-ray diffractometry (XRD, Empyrean, PANalytical B.V. device, ALMELO) and CuKα radiation source, and analysed using HighScore Plus software with ICDD database. The XRD was operated at 45 kV and 40 mA with the scanning rate of 3° 2θ/min. Microstructures were investigated for both synthesized powders and deposited coatings with scanning electron microscope (SEM, Jeol JSM 6360LV) and field emission scanning electron microscope (FESEM, Zeiss ULTRAplus) together with energy-dispersive spectrometer (EDS, Oxford Instruments, $XMax^N$ silicon drift detector). For imaging, secondary electron (SE) detector or angle selective backscattered electron (AsB) detector was used. For microstructural analyses, metallographic cross sections were prepared by casting cut sections of the specimens in Epofix cold setting resin under reduced pressure. The casts were then ground, polished and carbon coated for electrical conductivity. Electron backscatter diffraction (EBSD) system (Oxford Instruments, Symmetry EBSD detector based on CMOS technology with AZtecHKL software) integrated into FESEM was employed for crystal structure analysis. The cross-sectional EBSD samples were prepared by moulding the sections of specimens to epoxy followed by grinding and polishing down to the final finish by colloidal silica suspension (0.04 µm). After the final polishing, the samples were removed from epoxy.

The thermal behaviour of agglomerated powders was studied using thermogravimetric analysis (TG, Netzsch STA449 F1 Jupiter) giving a simultaneous differential scanning calorimetry (DSC) signal in order to investigate the differences in raw materials behaviour during the heat treating process. The tests were conducted in air atmosphere in a temperature range from 40 to 1200 °C with the heating rate of 10 °C/min. The final temperature was maintained for 1 hour before cooling the powders to the room temperature. A qualitative mass spectrometer (QMS, Netzsch QMS 403 D Aeolos) coupled directly to the TG device exhaust was used for evolved gas analysis.

The physical properties of synthesized powders were investigated. Particle size distributions for the powders were determined with laser diffractometer (Malvern Mastersizer). In addition, apparent densities of the powders were measured using hall flow tester 25 ml cup test.

Electric insulation properties of the coating samples were measured using breakdown voltage method. Prior to the measurements, coating thicknesses were measured with a magnetic measuring device (Elcometer 456B) from the electrode contact points. Breakdown voltage electrode areas (Ø=11 mm) and silver electrodes (Ø=11 mm) were painted on the coating surface as described in [9]. Silver paint penetration into the coating has been studied from cross-sectional images taken by optical microscope, and it has been observed that the utilized silver paint does not penetrate into the coating [9]. After painting the electrodes, the samples were first dried at 120 °C for two hours, followed by conditioning in a climate room at 20 °C/RH 20% for at least 12 h before the measurements. The breakdown measurements were performed in the climate room at 20 °C/RH 20%. In the breakdown tests, a stainless steel rod electrode (Ø=11 mm, edge rounding 1 mm), was placed on the top of a coating surface while the steel substrate of the sample acted as the other electrode. DC breakdown voltage measurements were performed by utilizing linearly increased DC voltage (ramp rate of 100 V/s throughout the test) [9]. The voltage source control and data recording was performed using a LabVIEW-based software [9]. The voltage source was Spellman SL1200 (*Umax*=20 kV) and the voltage level was measured using a resistive voltage divider (Spellman HVD-100-1, divider ratio 10000:1) [9]. Dielectric breakdown strength (DBS) of a coating was calculated by dividing the breakdown voltage by the corresponding coating thickness at the painted electrode (Ø=11 mm) location. Seven measurements were performed per each coating.

Hardness of the coatings was measured with hardness tester (DuraScan 20 Struers) and a Vickers intender. Sand abrasion tests by a rubber wheel tester were performed using quartz sand with the particle size of 0.32 mm and the feed of 350 g/min. A static contact force of 45 N against the rubber wheel, 233 mm in diameter, was used. Prior to the wear tests, the surfaces of samples were ground with a P1200 grinding disk to eliminate the effect of as-sprayed surface quality. Two samples per

coating were tested and their mass loss was measured at four time intervals (5, 10, 20, and 30 min) to ensure the linear wear performance during rubber wheel abrasion tests. After the tests, the surfaces and cross sections of the worn surfaces were investigated with SEM. The cross sections were prepared with focused ion beam SEM (FIBSEM, Zeiss Crossbeam 540) first by depositing a platinum (Pt) protection layer on top of the region of interest and then using gallium (Ga) ions to mill the cross-section under the Pt covering layer. Prior to FIBSEM studies, the samples were carbon-coated to avoid the sample charging during the milling process.

3. RESULTS AND DISCUSSION

3.1. POWDER CHARACTERIZATION

3.1.1 Microstructure

Figure shows X-ray diffraction (XRD) patterns for the synthesized powders. As identified by XRD patterns, all synthesized powders revealed $MgAl_2O_4$ spinel as the main crystalline phase. Thus, the synthesis of $MgAl_2O_4$ spinel was successful for all the powder mixtures shown in Table . For Reference powder, and the intermediate compositions, SC30 and SC60 powders, $MgAl_2O_4$ spinel peaks were the only peaks observed for crystalline phases. Nevertheless, XRD pattern for 100% secondary composition powder, SC100, showed additionally to the peaks related to the spinel phase minor unidentified peaks at the 2theta values of 28°, 33° and 61°. Thus, only the most impure SC100 powder introduced extra peaks in addition to $MgAl_2O_4$ spinel peaks in the XRD curve. Probably these minor crystalline phases were also present in SC30 and SC60 powders, but their amounts were too low to be detected by XRD. Vusikhis et al. [21] suggested that in the case of ferroan magnesite, during the decarbonisation of magnesite, both MgO and spinel $MgFe_2O_4$ were formed. Thus, it is likely that powders synthesized from mining tailings sample: SC30, SC60 and SC100, contained $MgFe_2O_4$ phase in addition to the $MgAl_2O_4$ phase. Spinel $MgFe_2O_4$ is also known as magnesioferrite. XRD patterns for $MgAl_2O_4$ and $MgFe_2O_4$ are almost identical, thus according to XRD data it is hard to draw any conclusions about the presence of $MgFe_2O_4$ in the synthesized powders. One possibility is also that there is some dissolution between $MgAl_2O_4$ and $MgFe_2O_4$

Talc ore mining tailings sample contains also silicate minerals as impurities, thus it was assumed that traces of these silicate minerals could also be found in secondary raw material containing powders. As mentioned, XRD pattern for SC100 powder contained minor unidentified peaks at the 2theta values of 28°, 33° and 61°. Another possible explanation for these unidentified peaks is that they were related to some complex silicates formed from the elements which were not dissolved into the $MgAl_2O_4$ spinel. Figure, XRD patterns, revealed also that differences in the widths of $MgAl_2O_4$ peaks exist. This indicates that there were differences in crystal sizes between the 100% secondary SC100 powder and the remaining three powders: Reference, SC30 and SC60. SC100 powder had the most narrow peaks, indicating a relatively more coarse crystal size than the other powders.

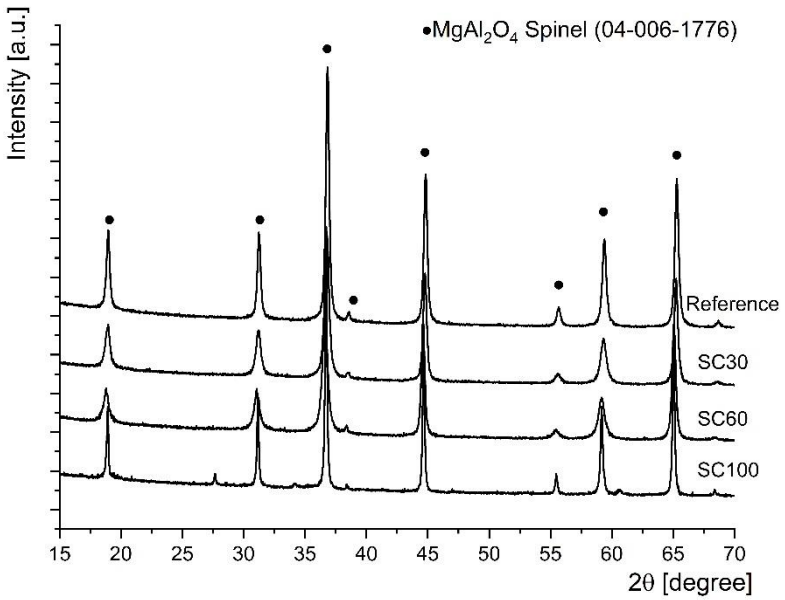

Figure 1. XRD patterns for synthesized powders Reference, SC30, SC60 and SC100.

Figure 2 (a-d) shows the surface morphology and Figure 3 (a-d) the cross-sectional images of the synthesized powders. Figures revealed clear differences in the primary particle size of agglomerated powders. Agglomerates of Reference powder were formed of very fine-grained particles evenly distributed all through the agglomerates. In turn, SC100 powder consisted of much larger primary particles which were essentially dense but formed a coarse agglomerate skeleton. FESEM-EDS analyses revealed that SC100 contained also the traces of Si (~2 wt.%) and Fe (~3 wt.%), which support the two explanations given for extra peaks in the XRD curve. Similarly, the traces of Si and Fe were detected for also other secondary raw materials containing powders SC30 and SC60. However, according EDS analyses, it is challenging to draw any definite conclusion about Si and Fe distribution because of the complexity of microstructural details, fine crystal size as compared to electron beam size and analysis spot dimension exceeding the crystal detail size. Structurally, powders SC30 and SC60 were closer to Reference powder than 100% secondary powder SC100, with essentially a small primary particle size (consistent with XRD data). Nevertheless, SC30 powder (Figure 3b) contained slightly larger pores than Reference and SC60 powders but the difference of SC30 compared to SC60 and Reference powder is quite marginal. This is resulting most probably from the poorer powder processing rather than the chemical composition in SC30 powder. All the studied powder mixtures were processed with similar processing parameters. As mentioned, there was notable difference in the particle sizes, dispersion and chemistry of the raw material powders.

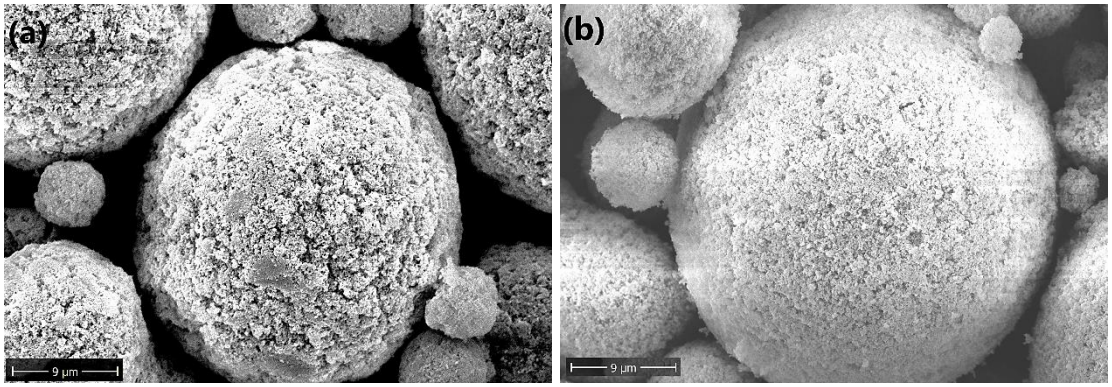

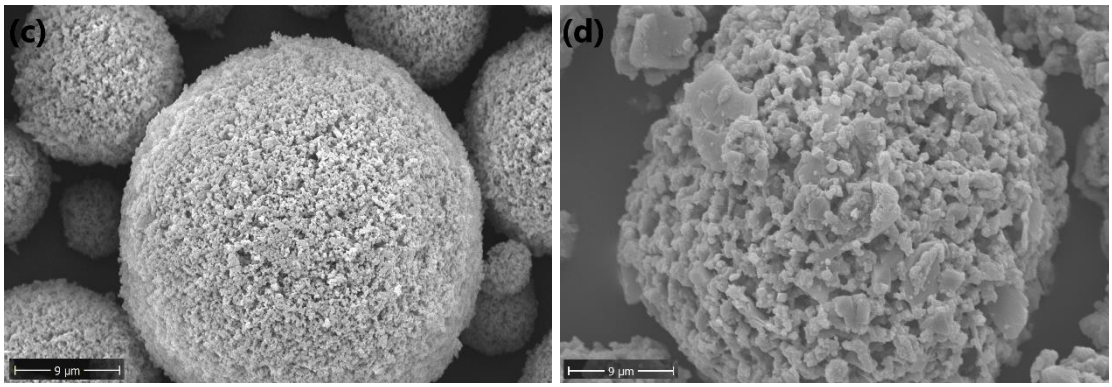

Figure 2. SEM (SE) images showing the powder morphology for powders (a) Reference (b) SC30 (c) SC60 and (d) SC100.

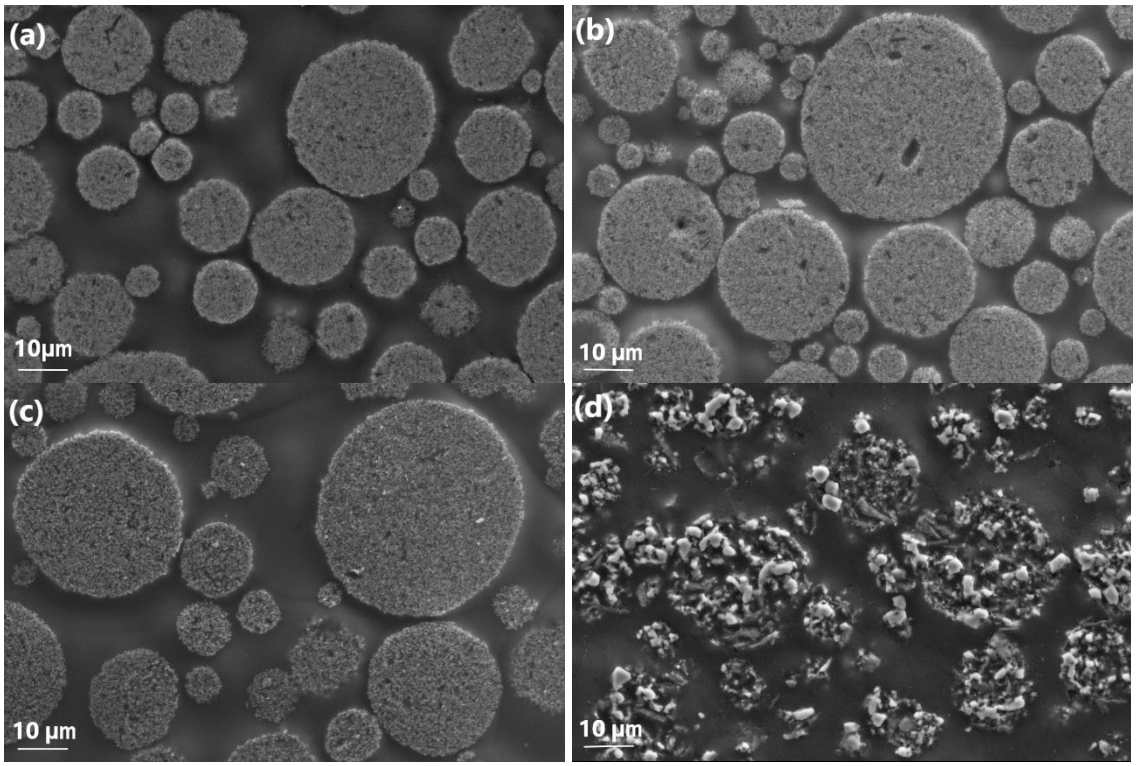

Figure 3. Cross-sectional FESEM (AsB) images for powders (a) Reference (b) SC30 (c) SC60 and (d) SC100.

3.1.2 Thermal behaviour

Thermal behaviour of the agglomerated powders was studied using TG/DSC/QMS in order to investigate the raw materials response to the heat-treatment step aiming at synthesizing $MgAl_2O_4$ powders. Figure 4 presents the TG/DSC/QMS curves for agglomerated powders in the case of (a) Reference powder (b) SC30 powder (c) SC60 powder and (d) SC100 powder.

In the case of Reference powder, the powder mixture consisted only commercial pure starting materials, MgO and AlO(OH). DSC curves for Reference powder in Figure (a) revealed an exothermic peak at 367°C, relating to the dehydration of magnesium hydroxide $Mg(OH)_2$ which introduced water evaporation, detected in evolved gas curve and accounting for approximately 13%

weight loss in TG curve (Equation 1). Magnesium hydroxide was likely formed from starting material source in the powder mixture, MgO, by the reaction with water during the spray-drying step. Another exothermic peak was seen approximately at 500°C, relating to the dehydration of another starting material in the powder mixture, aluminium oxide hydroxide, AlO(OH). This transformation accounts for approximately 9% weight loss in TG curve due to water release, as indicated by evolved gas curve (Equation 2) resulting formation of Al_2O_3. Similar values for dehydration temperatures have been presented in literature for $Mg(OH)_2$ [23] and for AlO(OH) [24]. Prior to these reactions, evaporation of water occurred, relating to the removal of moisture from agglomerated powders. Additionally, at the peak temperature of 361°C, evaporation of carbon dioxide, CO_2, was detected relating to the removal of the organic binder used in spray drying. Similar CO_2 release at approximately the same temperature range was detected in all powder mixtures relating to removal of the organic binder. After completion of the dehydration of aluminium oxide hydroxide (at 500°C), the reaction between Al_2O_3 and MgO was possible, resulting in $MgAl_2O_4$ formation (Equation 3). An exothermic peak detected at 1099 °C was probably related to the spinel evolution. Magnesium aluminate spinel formation has been reported to be a heat releasing reaction [25].

$$Mg(OH)_2 \rightarrow MgO + H_2O \quad (1)$$

$$2AlOOH \rightarrow Al_2O_3 + H_2O \quad (2)$$

$$Al_2O_3 + MgO \rightarrow MgAl_2O_4 \quad (3)$$

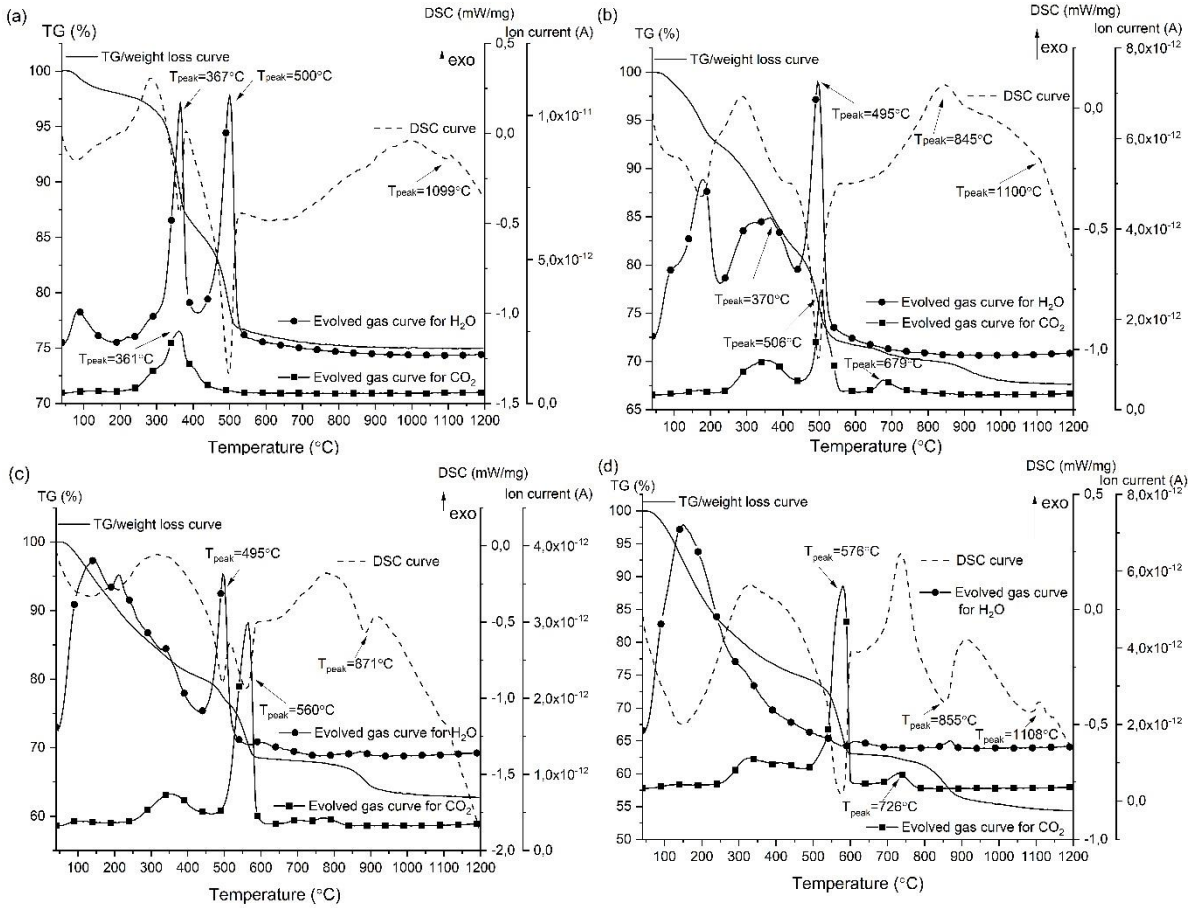

Figure 4. TG/DSC/QMS curves for (a) Reference powder (b) SC30 powder (c) SC60 powder and (d) SC100 powder.

In the case of SC100 powder, the powder mixture consisted only impure starting materials, talc ore mining tailings sample and secondary $Al(OH)_3$ precipitate. The TG/DSC/QMS curves shown in Figure (d) revealed transformations as response to the heat-treatment for these impure raw materials showing different behaviour than the pure raw materials in the case of Reference powder shown in Figure 4 (a). Below 500°C, the TG curve in Figure 4 (d) revealed already 25% weight loss related to transformations in DSC curve, most probably relating to starting material in the powder mixture, $Al(OH)_3$ precipitate, dehydration. Živković and Dobovišek [26] have studied the aluminium hydroxide dehydration and they suggest it proceeds according to the following mechanisms (Equation4, Equation5):

$$2Al(OH)_3 \rightarrow 2AlOOH + 2H_2O \qquad (4)$$

$$2AlOOH + H_2O \rightarrow Al_2O_3 + 2H_2O \qquad (5)$$

They suggested that both reactions proceed in the diffusion region, the first (Reaction 4) up to the temperature of 253°C and the second (Reaction 5) up to 427°C. Thus based on the water evaporation detected in evolved gas curve it could be confirmed that 25% weight loss in Figure 4 (d) below 500°C was related to these $Al(OH)_3$ dehydration reactions resulting in the formation of Al_2O_3.

According to mineralogical analysis, the talc ore mining tailings sample was composed 80% of magnesite $MgCO_3$, about 9.4% of talc $Mg_3Si_4O_{10}(OH)_2$ and about 4.9% of chlorite $(Mg,Fe)_3(Si, Al)_4O_{10}$. As mentioned in raw material section, the magnesite in talc ore tailings was not stoichiometric $MgCO_3$ but has a varying amount of iron substituting Mg in the lattice, being likely breunnerite rather than pure magnesite. Vusikhis et al. [21] have studied the kinetic features decarbonisation of breunnerite, the magnesite mineral where iron carbonate content lies between 5% and 30%. They suggested that carbonates begun to dissociate in a temperature range of 500–584°C. They detected two endothermic transformations in the DSC curve (beginning above 584°C, with the maxima at 664°C and 710°C), connected with the release of CO_2. They explained the presence of two separate peaks in the DSC curve by the following reactions, forming besides MgO the spinel $MgFe_2O_4$ (Equation6):

$$(Mg_{1-x}Fe_x)CO_3 = (Mg_{1-x}Fe_x)O + CO_2, 2(Mg_{1-x}Fe_x)O + 0.5xO_2 = (2-3x)MgO + xMgFe_2O_4 \quad (6)$$

Similarly to observations by Vusikhis et al. [21], DSC curve for SC100 powder in Figure (d) revealed two transformations, related to the peaks in CO_2 evaporation curve at the temperatures of 579°C and 726°C. These transformations could thus be linked with ferrous magnesite decarbonisation (Reaction 6) being present in the talc ore mining tailings sample. SC100 powder showed weight losses again above 800°C, connected with water evaporation in evolved gas curve. This transformation was most probably associated with the decomposition of hydrated magnesium silicates that were present as impurities in the mining tailings sample. Eventually at 1108 °C, an exothermic peak was detected, probably related to the formation of magnesium aluminate spinel by the reaction between magnesium oxide formed from tailings sample magnesite and aluminium oxide formed from $Al(OH)_3$ precipitate. Thus the main reaction between the starting materials was taken place between the alumina Al_2O_3 formed from $Al(OH)_3$ precipitate and the MgO formed from the tailings sample magnesite $MgCO_3$ resulting in $MgAl_2O_4$ phase formation. The impurities were most probably concentrated in spinel $MgFe_2O_4$ phase as suggested by Vusikhis et al. [21] and the magnesium silicates phases as residues.

In the case of SC30 and SC60 powders, the powder mixtures consisted both commercial and secondary sources of starting materials, approximately 30% secondary raw materials in SC30 powder and approximately 60% in SC60 powder. For that reason, TG/DSC/QMS curves for SC30 powder in Figure (b) and SC60 powder in Figure (c) disclosed transformations related to the dehydration of pure $Mg(OH)_2$ and AlO(OH) similarly than for the Reference in Figure 4 (a). Additionally also transformations related to impure raw materials, talc ore mining tailings sample and

secondary $Al(OH)_3$ precipitate were detected similarly than for the SC100 powder in Figure 4 (d). However, as a difference, decarbonization temperatures of magnesite $MgCO_3$ were lower for powder mixtures, SC30 and SC60, with pure raw materials present as compared to only 100% secondary raw materials containing SC100 powder.

3.1.2 Physical characteristics

Table 6 presents particle size distributions for agglomerated powders, measured with laser diffractometer. Along with the particle size distributions, the density values measured with hall flow tester are given. Particle size distributions for all agglomerated powders were relatively similar with d10 of approximately 10 µm and d90 of 40 µm, thus all were suitable for APS spraying. In density values, a clear difference was detected between the powders. Only secondary raw materials containing powder SC100 featured almost double density values as compared to others powders. This was mostly due to the coarser primary particle size, as disclosed by SEM studies, resulting in a better packing. Conversely, very fine particles of MgO and AlO(OH) caused loose packing of the remaining powders (Reference, SC30 and SC60). However, as the density of the spinel is from 3.5 to 4.0 g/cm^3, all powder density values indicate high porosity level in the powder agglomerates. This is also supported by SEM studies.

Table 6. Characteristics of the synthesized (heat treated) powders.

Powder code	**Particle size distribution d10-d90 [µm]**	**Apparent density [g/cm^3]**
Reference	11.9 - 44.8	0.52±0.01
SC30	7.1 - 37.4	0.43±0.02
SC60	12.0 - 45.0	0.40±0.02
SC100	9.9 - 42.6	0.86±0.03

3.2 COATING CHARACTERIZATION

3.2.1 Microstructure

Figure shows the XRD patterns for APS sprayed coatings. For all coatings, only cubic $MgAl_2O_4$ spinel phase was observed as the crystalline phase. XRD pattern revealed that secondary raw material containing coating SC100 coating and SC60 coating were partly amorphous. The intensities of crystalline spinel peaks were highest for Reference coating and the peak intensities decreased with increase in the relative amount of secondary raw materials (i.e., impurity content in raw materials). Similarly, spinel peaks shifted from the original 2θ position following the same order. The intensity decrease was probably due to both increased amount of amorphous phase and less perfect structure of the crystalline phase. Similarly, the shifting of XRD peaks was likely the result of impure composition, i.e., distortion of the lattice due to atomic size discrepancy. The unidentified small peaks that were detected in the XRD pattern for only secondary raw material containing SC100 powder (Figure d) were not any more visible in the pattern for the corresponding coating. Explanations for this are that this unidentified phase disappeared by dissolution to the spinel phase or to the amorphous glass phase in the coating. This dissolution may also be responsible to the spinel peak shifting. As the plasma spraying process involves the presence of melt, which is not present in powder synthesis, this kind of dissolution is plausible.

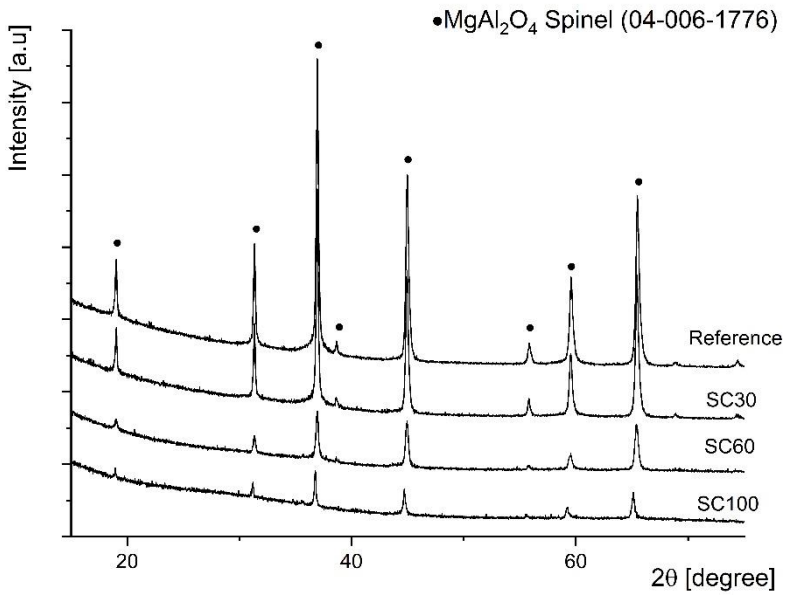

Figure 5. XRD patterns of the APS coatings Reference, SC30, SC60 and SC100.

Figure 6 shows cross-sectional FESEM images of the APS sprayed coatings for (a-c) Reference, (d-f) SC30, (g-j) SC60 and (i-k) SC100. The Reference was characterized by a lamellar microstructure typical of APS deposited coatings. Indeed, the formation of coatings by APS technique occurs by stacking the lamellae one by one, resulting from the impact, flattening, and finally solidification of the colliding molten particles [27]. The lamellas were crystalline, but some inter-lamellar areas contained a small amounts of amorphous phase. Crystalline lamella thickness was in the order of 1 to 4 µm, but amorphous sections between the crystalline lamellas were only 1 µm or less in thickness. Coating SC30 (Figure 6 (d-f)) featured similar lamellar microstructure of the crystalline phase, but the amorphous sections between the lamellas were essentially thicker and more frequent. Microstructures of coatings SC60 (Figure 6 (g-j)) and SC100 ((Figure 6 (i-k)) revealed the presence of high amount of the amorphous phase. Based on FESEM investigations, SC100 coating had the highest amount of amorphous phase in the structure (seen as the darker grey contrast in FESEM images), which was already observed in XRD pattern for the coating (Figure). Crystalline phase was concentrated on separate areas with a fine structure and seen in lighter grey contrast than the amorphous phase in FESEM images. SC100 coating also contained some lamellar areas, which had a similar morphology as in Reference coating. Due to the complex shape and small thinness, it was not possible to reliably analyze and identify the chemistry of the phases.

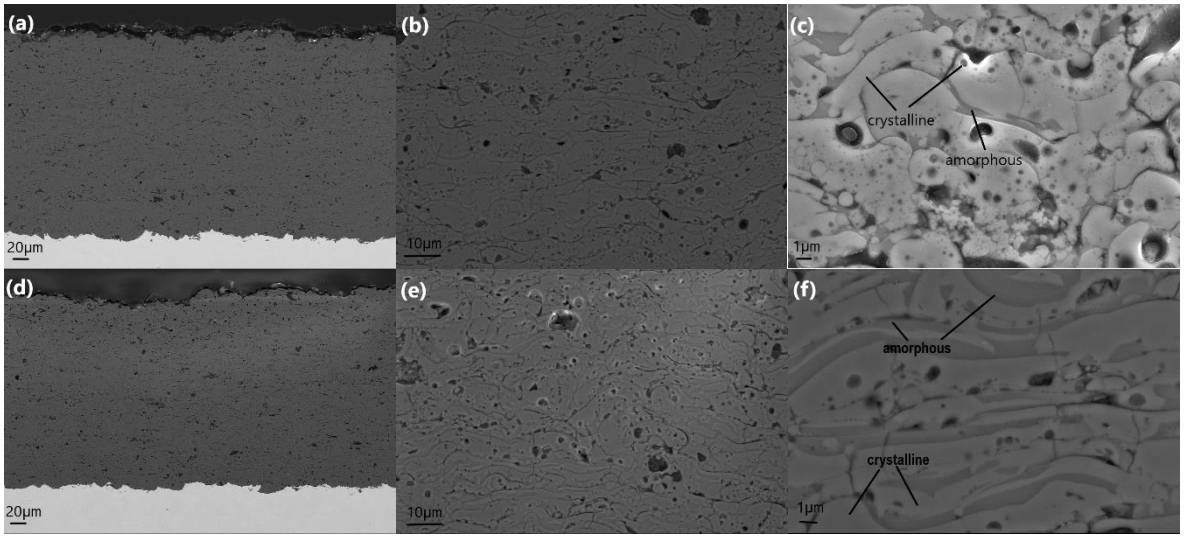

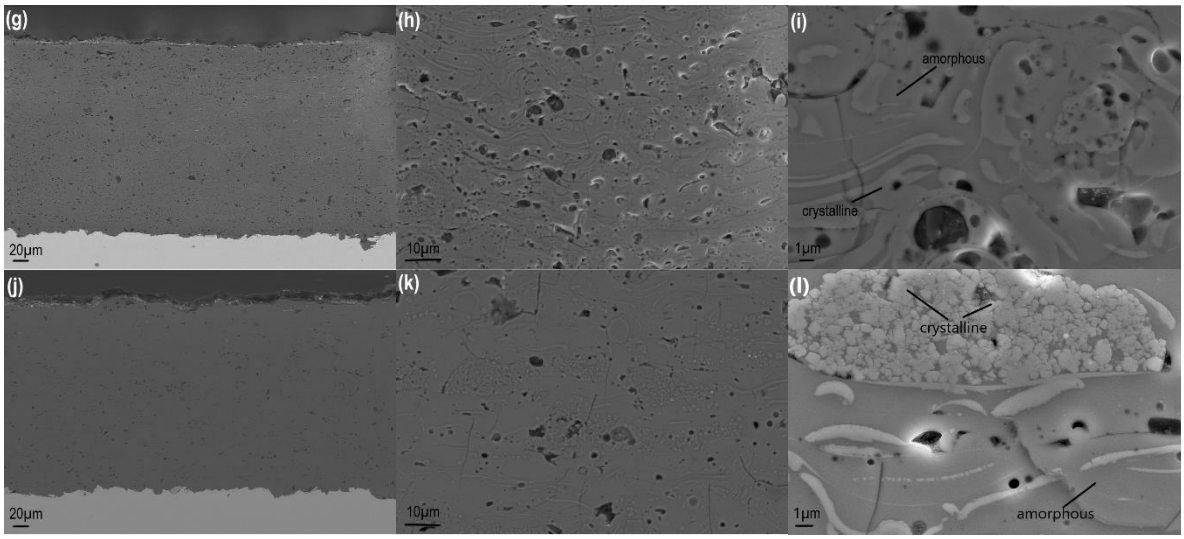

Figure 6. FESEM (SE or AsB) images of the APS-coatings cross-sections for (a-c) Reference coating (d-f) SC30 coating (g-i) SC60 coating and (j-l) SC100 coating.

The porosity values of studied APS coatings were defined by image analysis in Figure 6 shown FESEM micrographs using ImageJ software. The average porosity values defined were the following: for Reference coating 4.9±1.0 %, for SC30 coating 6.8±1.0 %, for SC60 coating 6.3±0.6 % and for SC100 coating 3.5±0.4 %. As detected in FESEM images of the Reference coating in Figure 6 (a-c) the lamellas were crystalline, but some inter-lamellar areas contained small amounts of amorphous phase. This was confirmed by FESEM-EBSD investigations shown in Figure 7. In the EBSD results, a band contrast (BC) map represents the quality of the Kikuchi diffraction pattern for each measurement pixel. In the BC map, bright signifies that the pattern quality is good, it can be indexed and crystal orientation can be determined. Black/dark grey signifies that the pattern cannot be indexed for example due to amorphous material. Here, also the nonconductive sample complicates the indexing especially in the edges of the crystalline lamellas. The colours in the inverse pole figure (IPF) maps (Z direction) correspond to the crystallographic orientations of $MgAl_2O_4$ parallel to the observed plane as indicated by the coloured stereographic triangle, i.e. an IPF colouring key.

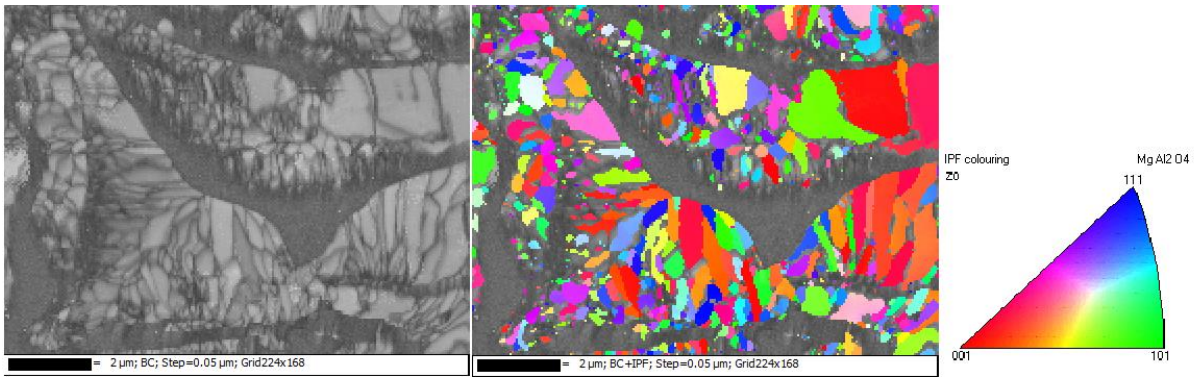

Figure 7. BC map and inverse pole figure (IPF) map superimposed on the BC map collected from Reference coating. The colours in the IPF maps correspond to the orientations parallel to the observed plane as indicated by the IPF colouring key.

3.2.2 Properties and performance

Table 7 presents the values of dielectric breakdown strengths for the studied coatings. Results revealed that breakdown strength values for all coatings, Reference, SC30, SC60 and SC100 were at the comparable level, at about 20 V/µm, considering the deviation in the results. The reported values are close to the DC breakdown strengths values of alumina and spinel coatings reported in literature [7] [8] [9] [10] [28][29].

According to results presented, the direct relation between the raw material chemical composition and the resulting breakdown strength values cannot be established. The thermal sprayed coatings manufactured using $MgAl_2O_4$ powder synthesized from secondary sources, talc ore tailings sample and $Al(OH)_3$ precipitate show similar level of breakdown strength values than coatings manufactured using $MgAl_2O_4$ powder synthesized from pure MgO and AlO(OH) sources. The electrical insulation capability was not decreased by the presence of impurities in raw materials. However, the deviation in the breakdown strength values was higher for secondary raw material based coatings. Also, for SC60 coating, slightly lower breakdown strength values than for the remaining three coatings were recorded. Most probable explanation for these lower breakdown strength values could be resulted from the higher amount of defects and porosity level in the coating as shown in SC60 coating microstructure in Figure 6 (g-j).

Table 7. Dielectric breakdown strength values for the coatings.

Coating code	Dielectric breakdown strength (V/µm)
Reference	23.0 ± 1.5
SC30	22.6 ± 1.4
SC60	18.1 ± 2.1
SC100	24.2 ± 3.8

Table 8 shows both the hardness values of the coatings and the results from their rubber wheel abrasive wear tests. Hardness results revealed that all the coatings that included secondary raw materials: SC30 coating, SC60 coating and SC100 coating were characterized by the hardness values approximately 20% lower than the Reference coating with pure commercial raw materials. Surprisingly, the differences between the three secondary raw materials containing coatings were only negligible, thus independent of the relative amount of secondary raw materials in the composition. These results suggest that the thermal sprayed coatings manufactured using $MgAl_2O_4$ powder synthesized from pure MgO and AlO(OH) resulted in higher hardness value and impurities in chemical composition of the starting materials decrease the hardness value.

Table 8. Hardness of and wear test results for the coatings.

Coating code	Hardness, HV 0.3kg	Weight loss [mg]			
		5min	10min	20min	30min
Reference	885±63	100± 3.3	-	-	-
SC30	670±70	164±3.6	-	-	-
SC60	684±85	96±10	-	-	-
SC100	687±50	17±1.6	33±3.5	53±3.3	73±7.2

In abrasive wear tests, the specimens of Reference coating, SC30 coating and SC60 coating were worn through already after 5 min test duration. The weight losses after 5min test duration for the Reference coating and SC60 coating specimens were approximately 100 mg taking into account the deviation in the results. The weight loss for SC30 coating specimen after 5 min test duration was higher than for Reference coating and SC60 coating specimens. The most probable reason for that is resulting from the higher porosity level detected for SC30 powder due to poorer processing, discussed in Powder Characterization section. On the contrary, the wear rate was considerably lower for 100% secondary raw material based SC100 coating than all other studied coatings. For SC100 coating specimens the weight loss detected after 5 min test duration was 17 mg and after 30 min test duration only 73 mg. Thus for SC100 coating specimens the weight loss is lower after 30 min test duration than that all other studied coatings specimens after 5 min test duration. Because only 100% secondary raw material based SC100 coating resulted lower wear rate than all other studied coatings, any evident relation between the wear results with the starting composition cannot be given. It is suggested that the different structure of the coatings, particularly the high degree of amorphous phase binding the separate crystalline $MgAl_2O_4$ clusters, causes the higher abrasive wear resistance of the 100% secondary raw material based coating by changing the wear mechanism. These results suggest that the coating hardness was not the only decisive factor for the abrasive wear resistance of the coating, as the hardest of the coatings (Reference) had a wear performance comparable to that of lower-hardness coatings (e.g., SC30). Conversely, the coating with the highest wear resistance, SC100 coating, featured the same hardness as the two coatings with much poorer wear resistance (SC30, SC60).

The worn surfaces were investigated after the abrasion wear tests using FESEM (top views) in Figure 8 (a) for the Reference and in Figure 8 (b) for the 100% secondary raw material based SC100 coating. The wear morphologies of the coatings, Figure 8, well reflected the results from the wear tests. For the Reference coating the wear tracks featured high surface roughness. The large smooth area in the middle of Figure 8 (a) indicates that a removal by lamella-by-lamella mechanism is likely. In the case of SC100 coating in Figure 8 (b), the wear surface was much smoother than for Reference coating, indicating that material losses occurred through the removal of only small fractions of the coating at a time and equally in all areas of the coating.

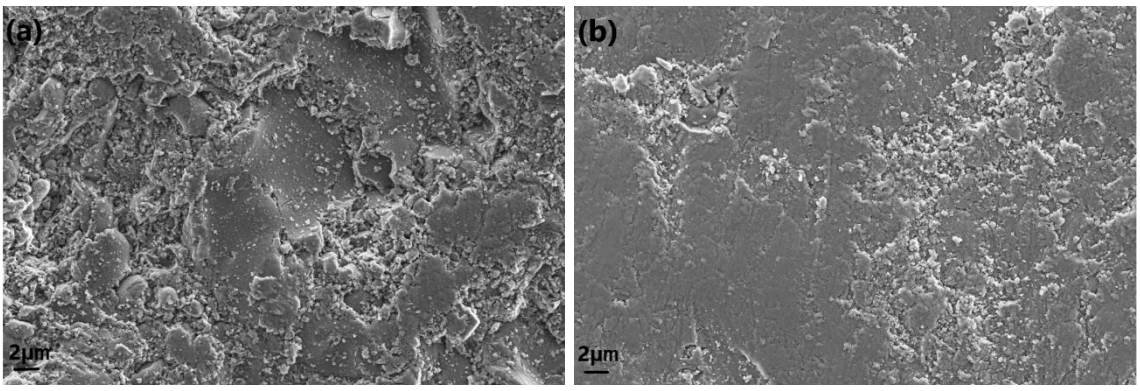

Figure 8. FESEM (SE) images of the worn surfaces of coatings (a) Reference and (b) SC100.

The worn surfaces were investigated also using FIBSEM (cross-sectional views) shown in Figure 9 for (a-b) Reference coating and (c-d) SC100 coating. For Reference coating Figure 9 (a-b), the cracks were often connected through the lamellar structure, which caused the removal of large pieces of the coating when exposed to abrasive wear. This suggests that the lamella boundaries may be the weak point of the material under abrasive wear. On the contrary, in secondary raw material based coating SC100 Figure 9 (c-d) there were also visible cracks but these were not systematically connected, thus when exposed to abrasive wear, material losses occurred only locally and mass losses were lower than for Reference coating. As detected in the microstructure investigations of APS sprayed coatings, SC100 coating was highly amorphous, with crystalline spinel phase in the structure being concentrated on separate clusters surrounded by the amorphous phase.

The amorphous phase binds the individual areas of the crystalline phase together thus there is no typically a direct connection between the crystalline areas. In all other coatings: Reference, SC30 and SC60, the crystalline phase forms the lamellar structure though the coatings. FESEM-EBSD investigations confirmed that in Reference coating, SC30 coating and SC60 coating, the crystalline phase was evenly distributed all through the structure but in SC100 coating, the crystalline phase was concentrated on separate clusters surrounded by the amorphous phase. Thus according to these results, the 100% secondary raw material based impurity-containing amorphous coating (SC100) was more resistant to abrasive wear as compared to pure $MgAl_2O_4$ coating. The presented microstructural results suggest that different structure of the coatings and the particularly the presence of amorphous structure causes the different behavior in abrasive wear test between the coatings by changing the mechanism for wear.

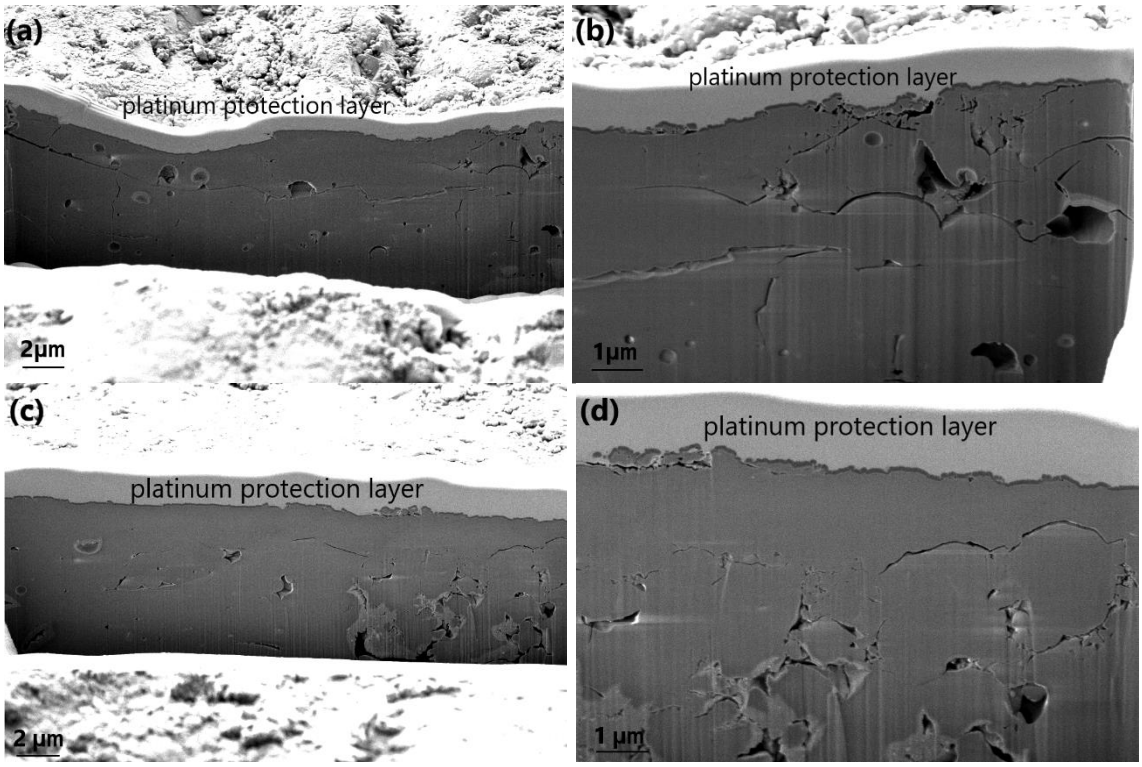

Figure 9. FIBSEM (SE) images of the worn surfaces for (a-b) Reference coating and (c-d) SC100 coating. Reference coating (a-b) is prepared from commercial pure raw materials and SC100 coating (c-d) using only secondary raw materials.

4. CONCLUSIONS

The following main conclusion could be drawn from the results:

- Agglomerated $MgAl_2O_4$ spinel based powders for thermal spraying, can be synthesized by spray drying and subsequent reaction sintering using secondary Mg (talc ore mining tailings) and Al (aluminium hydroxide precipitate from aluminium anodizing process) sources as raw materials.
- Atmospheric plasma spraying results in the formation of $MgAl_2O_4$ spinel coatings with the cubic $MgAl_2O_4$ spinel phase as only crystalline phase.
- The Reference coating prepared from commercial pure raw materials exhibits a lamellar microstructure, typical for APS spayed coatings.

- Coatings prepared from only secondary raw materials have a partly amorphous structure in which the amorphous phase binds together the separate crystalline $MgAl_2O_4$ clusters.
- The values of dielectric breakdown strength for the secondary raw material based coatings are at the same level, 24 V/µm, compared to pure magnesium aluminate coating, 23 V/µm, and close to the DC breakdown strengths of alumina and spinel coatings reported in literature. Thus, the electrical insulation capability is hardly affected by the impurities in raw materials.
- Abrasive wear test results reveal considerably lower wear rate for secondary raw materials $MgAl_2O_4$ spinel based coating than for the pure counterpart or the intermediate coating compositions. It is suggested that the different structure of the coatings, particularly the high degree of amorphous phase binding the separate crystalline $MgAl_2O_4$ clusters, causes the higher abrasive wear resistance of the secondary coating and changes the wear mechanism.
- The investigations of worn surfaces after abrasion tests reveal that the amorphous structure is more resistant to abrasive wear compared to lamellar structure. It seems to be possible that inferior mechanical properties of impure $MgAl_2O_4$ spinel is compensated by the introduction of glass phase in plasma spray coatings.
- These secondary raw materials could potentially substitute virgin raw materials in high-temperature electrical insulation ceramic coating applications.

Acknowledgement

The research has been supported by the Academy of Finland, project CeraTail funding decision # 292563 and by the Strategic Research Council at the Academy of Finland, project CloseLoop, funding decision #303453. A part of this work utilized Tampere Microscopy Center facilities at Tampere University. Thermal spray processing of the coatings were done at Thermal Spray Center Finland (TSCF) in Tampere. The authors would like to thank Ms. Hanna-Mari Sinilehto for participating in the experimental work and characterization and M.Sc Tommi Varis for coatings porosity determinations.

REFERENCES

[1] R. Dal Maschio, B. Fabbri, and C. Fiori, “Industrial Applications of Refractories Containing Magnesium Aluminate Spinel,” *Ind. Ceram.*, vol. 8, no. 3, pp. 121–126, 1988.

[2] I. Ganesh, “A review on magnesium aluminate (MgAl2O4) spinel: synthesis, processing and applications,” *Int. Mater. Rev.*, vol. 58, no. 2, pp. 63–112, 2013.

[3] G. Bertrand, C. Meunier, P. Bertrand, and C. Coddet, “Dried particle plasma spray in-flight synthesis of spinel coatings,” *J. Eur. Ceram. Soc.*, vol. 22, no. 6, pp. 891–902, 2002.

[4] M. Niittymäki, K. Lahti, T. Suhonen, and J. Metsäjoki, “Dielectric Breakdown Strength of Thermally Sprayed Ceramic Coatings: Effects of Different Test Arrangements,” *J. Therm. Spray Technol.*, vol. 24, no. 3, pp. 542–551, 2015.

[5] C. Petot, M. Ducos, and G. Petot-Ervas, “Thermal spray spinel coatings on steel substrates: Influence of the substrate composition and temperature,” *J. Eur. Ceram. Soc.*, vol. 15, no. 7, pp. 637–642, 1995.

[6] G. Mauer, R. Vaßen, and D. Stöver, “Thin and dense ceramic coatings by plasma spraying at very low pressure,” *Proc. Int. Therm. Spray Conf.*, vol. 19, no. January, pp. 773–778,

2009.

[7] F. L. Toma, S. Scheitz, L. M. Berger, V. Sauchuk, M. Kusnezoff, and S. Thiele, “Comparative study of the electrical properties and characteristics of thermally sprayed alumina and spinel coatings,” *J. Therm. Spray Technol.*, vol. 20, no. 1–2, pp. 195–204, 2011.

[8] M. Niittymaki, I. Rytoluoto, K. Lahti, J. Metsajoki, and T. Suhonen, “Role of microstructure in dielectric properties of thermally sprayed ceramic coatings,” *Proc. 2016 IEEE Int. Conf. Dielectr. ICD 2016*, vol. 2, pp. 1102–1105, 2016.

[9] M. Niittymaki, K. Lahti, T. Suhonen, and J. Metsajoki, “DC conduction and breakdown behavior of thermally sprayed ceramic coatings,” *IEEE Trans. Dielectr. Electr. Insul.*, vol. 24, no. 1, pp. 499–510, 2017.

[10] M. Niittymaki, T. Suhonen, K. Lahti, J. Metsajoki, and U. Kanerva, “Influence of humidity and temperature on the dielectric properties of thermally sprayed ceramic MgAl<inf>2</inf>O<inf>4</inf> coatings,” pp. 94–97, 2014.

[11] S. Sampath, J. Longtin, R. Gambino, H. Herman, R. Greelaw, and E. Toremy, “Direct-Write Thermal Spraying of Multilayer Electronics and Sensor Structures, Direct-Write Technologies for Rapid Prototyping Applications,” in *Direct-Write Technologies for Rapid Prototyping Applications: Sensors, Electronics, and Integrated Power Sources*, A. Pique and D. Chrisey, Eds. Academic Press, New York, 2002, pp. 261–302.

[12] S. A. Walling and J. L. Provis, “Magnesia-Based Cements: A Journey of 150 Years, and Cements for the Future?,” *Chem. Rev.*, vol. 116, no. 7, pp. 4170–4204, 2016.

[13] European Commission, “Annexes to the Report on Critical raw materials for the EU,” no. May 2014, 2014.

[14] U.S.G.S, “Mineral Commodity Summaries 2015 Mineral Commodity Summaries 2015,” *US Geol. Surv.*, p. 196, 2015.

[15] B. G. Lottermoser, *Mine Wastes (third edition): Characterization, treatment and environmental impacts*. 2010.

[16] M. Edraki, T. Baumgartl, E. Manlapig, D. Bradshaw, D. M. Franks, and C. J. Moran, “Designing mine tailings for better environmental, social and economic outcomes: A review of alternative approaches,” *J. Clean. Prod.*, vol. 84, no. 1, pp. 411–420, 2014.

[17] B. G. Lottermoser, “Recycling, reuse and rehabilitation of mine wastes,” *ELEMENTS*, vol. 7, pp. 405–410, 2011.

[18] M. . Räisänen, “Magnesiittirikastushiekan ympäristökelpoisuus,” 2004.

[19] S. Solismaa *et al.*, “Valorization of Finnish mining tailings for use in the ceramics industry,” *Bull. Geol. Soc. Finl.*, vol. 90, no. 1, pp. 33–54, 2018.

[20] A. Ismailov, N. Merilaita, S. Solismaa, M. Karhu, and E. Levänen, “Utilizing mixed-mineralogy ferroan magnesite tailings as the source of magnesium oxide in magnesium potassium phosphate cement,” *Constr. Build. Mater.*, 2019.

[21] A. S. Vusikhis, R. I. Gulyaeva, L. I. Leont’ev, L. A. Ovchinnikova, and E. N. Selivanov, “Kinetic features of breunnerite decarbonization,” *Russ. Metall.*, vol. 2016, no. 9, pp. 793–797, 2016.

[22] P. Vuoristo, “Thermal Spray Coating Processes,” *Compr. Mater. Process.*, pp. 229–276,

Jan. 2014.

[23] T. Yoshida, T. Tanaka, H. Yoshida, T. Funabiki, S. Yoshida, and T. Murata, “Study of dehydration of magnesium hydroxide,” *J. Phys. Chem.*, vol. 99, no. 27, pp. 10890–10896, 1995.

[24] S. J. Wilson, “The dehydration of boehmite, γ-AlOOH, to γ-Al2O3,” *J. Solid State Chem.*, vol. 30, no. 2, pp. 247–255, Nov. 1979.

[25] P. Orosco, L. Barbosa, and M. D. C. Ruiz, “Synthesis of magnesium aluminate spinel by periclase and alumina chlorination,” *Mater. Res. Bull.*, vol. 59, pp. 337–340, 2014.

[26] Ž. . Živković and B. Dobovišek, “Kinetics of aluminium hydroxide dehydration,” *J. Therm. Anal.*, vol. 12, no. 207, doi.org/10.1007/BF01909477, 1977.

[27] K. . (ed) Stern, *Metallurgical and Ceramic Protective Coatings*. Chapman & Hall, London, 1996.

[28] M. Niittymaki, K. Lahti, T. Suhonen, and J. Metsajoki, “Effect of temperature and humidity on dielectric properties of thermally sprayed alumina coatings,” *IEEE Trans. Dielectr. Electr. Insul.*, vol. 25, no. 3, pp. 908–918, 2018.

[29] F. L. Toma *et al.*, “Comparison of the microstructural characteristics and electrical properties of thermally sprayed Al 2O 3 coatings from aqueous suspensions and feedstock powders,” *J. Therm. Spray Technol.*, vol. 21, no. 3–4, pp. 480–488, 2012.